Check for updates

Enhanced gas sensing performance of perovskite YFe₁₋ₓMnₓO₃ by doping manganese ions†

Aerzigu Xukeer, [a] Zhaofeng Wu, *[a] Qihua Sun,[a] Furu Zhong,[b] Min Zhang,[a] Mengqiu Long *[c] and Haiming Duan*[a]

Perovskite $YFe_{1-x}Mn_xO_3$ with a hierarchical structure were prepared by a simple hydrothermal method and used as gas sensing materials. The structure, morphology and composition of $YFe_{1-x}Mn_xO_3$ were investigated using X-ray diffraction, transmission electron microscopy, scanning electron microscopy and X-ray photoelectron spectroscopy. The gas sensing test showed that all $YFe_{1-x}Mn_xO_3$ perovskites with different Mn doping concentrations displayed fast response and recovery characteristics to multiple analytes as well as good stability and recoverability. With the increase of Mn doping concentration, the response of $YFe_{1-x}Mn_xO_3$ to four kinds of target atmospheres first increases, then decreases. The sensing performance of $YFe_{1-x}Mn_xO_3$ is best when $x = 0.05$. Compared with pure $YFeO_3$, the responses of $YFe_{0.95}Mn_{0.05}O_3$ to 1000 ppm of CH_2O, C_2H_6O, H_2O_2 and 100% relative humidity were increased by 835%, 1462%, 812% and 801%, respectively. The theoretical detection limit of $YFe_{0.95}Mn_{0.05}O_3$ for H_2O_2 and CH_2O is 1.75 and 2.55 ppb, respectively. Furthermore, the possibility of buildings a sensor array based on $YFe_{1-x}Mn_xO_3$ with different doping concentrations was evaluated by principal component analysis and radar chart analysis. It is feasible to realize the visual and discriminative detection of the target analyte by constructing sensor arrays through radar chart analysis and database construction.

1. Introduction

Perovskites have a great effect in many domains, such as gas sensors.[1–4] Recently, a variety of perovskite structures based on ABO₃-type composites have been used as gas sensors due to their high stability and also their characteristics of sensitivity and selectivity.[4–6] Perovskite BaSnO₃ obtained from a simple wet chemical route was calcined at different temperatures and the gas sensing performance was studied in the presence of O₂, CO and NO₂ as a function of the temperature. The BaSnO₃ sensor shows a maximum sensitivity to O₂ and at 700 °C, to CO and NO₂ at 600 °C, respectively.[7] Traversa fabricated the thick films of LaFeO₃ and SmFeO₃ by screen-printing technology on alumina substrates with comb-type Au electrodes. The effect of temperature and humidity on the gas sensing performance of LaFeO₃ and SmFeO₃ to NO₂ and CO were studied and the presence of humidity does not affect the detection of NO₂ and CO.[8] The sensing properties of SrTiO₃ were regulated by the annealing temperature due to the change of the grain size of

SrTiO₃. The optimal relative resistance ($R_{nitrogen}/R_{20\%\ oxygen}$) value of 6.35 is obtained for the synthesized SrTiO₃ sample annealed at 400 °C and operating at 40 °C, which is much lower than that for the conventional metal oxide semiconducting oxygen gas sensors (300–500 °C).[9,10] Later, traditional metal oxide semiconductors or noble metal nanoparticles were used to form composites with perovskite materials to improve their gas sensing performance. Ruan synthesized porous core–shell PrFeO₃/α-Fe₂O₃ composites, realized a high gas response, low optimum operating temperature and superior selectivity to ethyl acetate gas. The response (R_{air}/R_{gas}) of the sensor based on PrFeO₃/α-Fe₂O₃ is 22.85 toward 100 ppm ethyl acetate at 206 °C, about 3 times higher than that of pristine α-Fe₂O₃ sensor. Besides, the sensor possesses a rapid response and recovery speed of 8 s and 9 s for detecting 100 ppm ethyl acetate.[2] Perovskite LaCoO₃ was synthesized by sol–gel method and functionalized by Ag nanoparticles. An improved sensitivity and selectivity to H₂S was observed for Ag/LaCoO₃ sensors, compared with pure LaCoO₃ sensor. The role of Ag nanoparticles in the selective sensitivity of Ag/LaCoO₃ composites to H₂S gas were unveiled using *in situ* infrared spectroscopy.[3] Mandayo prepared BaTiO₃–CuO films and annealed at different temperatures in order to test their electrical behavior by means of impedance measurements under different CO₂ concentrations (0–2000 ppm). Pt and Ag are tested as electrode materials and the influence of Ag as surface and multilayer additive for sensing response enhancement is also studied.[11]

ᵃSchool of Physics Science and Technology, Xinjiang University, Urumqi, Xinjiang 830046, P. R. China. E-mail: wuzf@xju.edu.cn; dhm@xju.edu.cn

ᵇSchool of Physics and Electronic Science, Zunyi Normal College, Zunyi, 563006, Guizhou, P. R. China

ᶜInstitute of Super-microstructure and Ultrafast Process in Advanced Materials, School of Physics and Electronics, Central South University, Changsha 410083, P. R. China

Compared with the composite method of improving the sensing performance of the perovskites, doping may be a simpler and more effective way to regulate the sensing properties of perovskites, which can be done synchronously in the process of synthesizing materials.[12,13] The cubic ABO_3 unit cell of perovskites contain a large 12-coordinated A cation centered between the corner-sharing BO_6 octahedra. The ABO_3 structure is favorable for cation substitution in either A, or B positions, which influences the electrophysical and chemical properties of the perovskite oxides. This means that the controlled doping of ABO_3 structure can effectively control the gas sensing properties of perovskites. Rothschild explored the sensing performances of $SrTi_{1-x}Fe_xO_{3-\delta}$ as oxygen sensors in lean burn engines and found that with the change of the molar ratio of Ti/Fe, the bandgap energy and gas sensing performance of the $SrTi_{1-x}Fe_xO_{3-\delta}$ material changed synchronously.[14] Among these perovskites, yttrium orthoferrite ($YFeO_3$) has attracted the attention of researchers due to their excellent magnetic, magneto-optical, physical and chemical properties originated by their ionic and electronic defects as well as structure distortions.[15–17] To the best of our knowledge, most previous studies on $YFeO_3$ have been focused on its photoluminescence, catalysts and magnetic properties,[18–22] but few have been reported on gas sensing. In terms of actual sensing requirements, controlling and monitoring the toxic, inflammable and explosive gases, such as formaldehyde (CH_2O), ethanol (C_2H_6O) and hydrogen peroxide (H_2O_2), is important for industrial production, indoor life and public safety.[13,23–25]

Doping can change the composition, carrier density and surface states of sensing materials, which is an effective strategy to regulate the structure and the gas-sensitive properties, as well as an important means to study the gas-sensitive mechanism of semiconductor materials.[26,27] In our work, the hierarchical $YFe_{1-x}Mn_xO_3$ was prepared by hydrothermal method and the substitution of Mn ions at Fe site was achieved, because of the close ionic radius of Mn^{3+} (0.580 Å), Mn^{2+} (0.670 Å) and Fe^{3+} (0.645 Å).[28,29] The effect of Mn doping on the gas sensing performances of $YFe_{1-x}Mn_xO_3$ to CH_2O, C_2H_6O and H_2O_2 has been studied. Furthermore, the possibility of building sensor array based on $YFe_{1-x}Mn_xO_3$ with different doping concentration was evaluated by principal component analysis (PCA) and radar chart analysis.

2. Experimental section

2.1 Material preparation

Yttrium nitrate hexahydrate $[Y(NO_3)_3 \cdot 6H_2O]$, iron(III) nitrate nonahydrate $[Fe(NO_3)_3 \cdot 9H_2O]$, manganese(II) chloride ($MnCl_2 \cdot 4H_2O$), and potassium hydroxide (KOH) are analytical reagents, purchased from Sinopharm Chemical Reagent Co., Ltd. $YFe_{1-x}Mn_xO_3$ ($x = 0$, 0.025, 0.05, 0.075 and 0.1) nanopowders were prepared by hydro-thermal method. First, 0.01 mol of $Y(NO_3)_3 \cdot 6H_2O$ and $Fe(NO_3)_3 \cdot 9H_2O$, and a certain amount of $MnCl_2 \cdot 4H_2O$ were weighed and dissolved in 30 ml of distilled water with stirring. Second, 0.75 mol of KOH as mineralizing agent was directly added into the above solution, the mixtures were then transferred to Teflon-lined stainless

steel autoclave and heated at 230 °C for 72 h. Third, the dark products were filtered and washed several times with distilled water to obtain crystals that are then dried in air.

2.2 Device fabrication and testing

The fabrication and testing of sensors are the same as the previous reports.[13,25] Specifically, sensors based on $YFe_{1-x}Mn_xO_3$ ($x = 0$, 0.025, 0.05, 0.075 and 0.1) were fabricated by coating the paste of $YFe_{1-x}Mn_xO_3$ on a ceramic substrate by a thin brush to form a sensing film on which silver interdigitated electrodes with both finger-width and inter finger spacing of about 200 μm was previously printed. The sensors based on $YFe_{1-x}Mn_xO_3$ ($x = 0$, 0.025, 0.05, 0.075 and 0.1) were defined as S1, S2, S3, S4 and S5, respectively. The sensor were dried at 25 °C about 24 h and then aged at 3 V in air for about 48 h to ensure the good stability. Gas sensing performance was measured by an electrochemical workstation (CIMPS-2, ZAHER ENNIUM) in a 25 °C test room controlled by air conditioning system. For the target vapor of different concentrations is prepared according to formula (1):

$$Q = \frac{1}{22.4 \times 10^6} \times \frac{V \times C \times M}{d \times \rho} \times \frac{273 + T_R}{273 + T_B} \qquad (1)$$

where: Q and V is the volume of the liquid to be taken and the volume of the test bottle, respectively; M is the molecular weight of the substance; d is the purity of the liquid; C is the concentration of the gas to be prepared; ρ is the density of the liquid; T_R and T_B is the test ambient temperature and the temperature in the test bottle. During the preparation of the target vapors by heating, the containers were sealed. After a certain concentration of vapors were generated, the sealed containers were placed at 25 ± 1 °C for about 2 h to reduce the temperature of the target vapors to 25 ± 1 °C. A constant potential of 3 V was applied across the sensor and the relative change of electric current when switching from air to the target gases was recorded by electrochemical workstation at room temperature. The response was defined as response $= \Delta I/I_R = (I_R - I_G)/I_R$, where I_R and I_G were electric current in the reference gas and the target gas, respectively. The response and recovery time was defined as the interval between when response reached 90% of its maximum and dropped to 10% of its maximum.[13]

2.3 Characterization

X-ray powder diffraction (XRD) measurement was carried out using powder XRD (Bruker D8 Advance, with Cu-Kα radiation operating at 40 kV and 40 mA). Field emission scanning electron microscopy (FE-SEM, S-4800, Hitachi, Japan) was used to investigate the surface morphology of $YFe_{1-x}Mn_xO_3$ ($x = 0.000$, 0.025, 0.050, 0.075 and 0.100). Transmission Electron Microscopy (TEM, FEI Tecnai G2 F20 S-TWIN) was used to characterize the morphology of $YFe_{1-x}Mn_xO_3$ ($x = 0.050$) sample. The surface elements and chemical states of the samples were examined using X-ray photoelectron spectroscopy (XPS, PHI 5000Versa Probe). The content of each element in the materials was measured by energy dispersive X-ray spectroscopy (EDS) and inductively coupled plasma emission spectrometer (ICP).

3.   Results and discussion

3.1   Morphology and structural properties

The surface morphologies of $YFe_{1-x}Mn_xO_3$ ($x = 0.000$, 0.025, 0.050, 0.075 and 0.100) investigated by SEM are given in Fig. 1. On the macro level, all the micron particles of $YFe_{1-x}Mn_xO_3$ are basically composed of a square sheet and two sides of the square sheet symmetrically growing hierarchical structures (Fig. 1a, d, g, j, m). At the micro level, the hierarchical structure on both sides of the square sheet is like a maze of long building units (Fig. 1b, e, h, k, n), and their morphology does not change with the increase of Mn doping. More detailed observation shows that the basic unit is a quadrangular prism with width of several hundred nanometers, length of several microns or even more than ten microns. One-dimensional structure of YFe_{1-x}-Mn_xO_3 facilitates the rapid transport and transfer of charges between one-dimensional quadrangle and target gas.[30,31] Moreover, there are some nanoparticles growing on the surface of the prism (Fig. 1c, f, i, l, o). This may provide a large surface area and active sites for the adsorption of the target gas, which
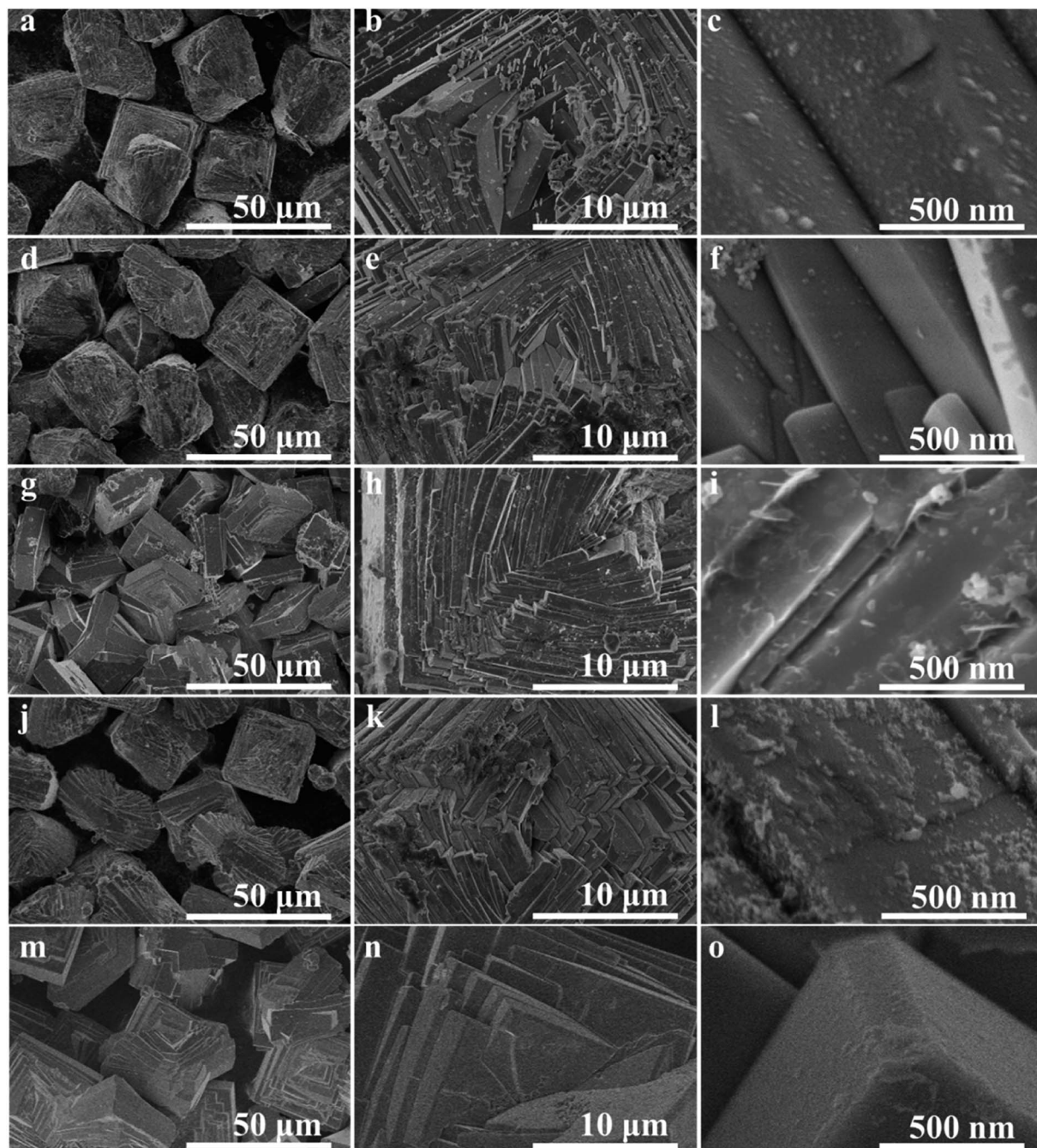

Fig. 1 SEM images of five samples (a–c) $YFeO_3$, (d–f) $YFe_{0.975}Mn_{0.025}O_3$, (g–i) $YFe_{0.95}Mn_{0.05}O_3$, (j–l) $YFe_{0.925}Mn_{0.075}O_3$, and (m–o) $YFe_{0.9}Mn_{0.1}O_3$.

is conducive to improving the gas sensing performance of the material.[32] In addition, it should be noted that when the doping amount of manganese ion reaches 10%, the hierarchical structure becomes less fine and the basic unit becomes wider, changing slightly the morphology of the $YFe_{1-x}Mn_xO_3$ materials.

XRD patterns of five $YFe_{1-x}Mn_xO_3$ doped with different amount of Mn are shown in Fig. 2a. The XRD investigation suggests that all these samples give rise to well-established peaks of orthorhombic perovskite structure with lattice constant $a = 5.5957$ Å, $b = 7.6046$ Å and $c = 5.2819$ Å (JCPDS no. 89-2609).[28,33,34] As shown in Fig. 2a, the typical diffraction peaks at 25.99, 31.98, 33.17, 33.94, 39.54, 47.31, 47.87, 48.91, 53.45, 57.73, 58.75, 60.24 and 76.017 can be ascribed to the (111), (200), (121), (002), (112), (202), (040), (212), (311), (321), (240) and (123) faces of orthorhombic $YFeO_3$, which are comparable to those reported in literature.[28,33,34] In the concentration range of 10%, with the increase of Mn doping concentration, the structure and crystal phase of $YFe_{1-x}Mn_xO_3$ materials have almost no change, and the pure $YFeO_3$ structure is still maintained. It should be pointed out that the intensity of the diffraction peak gradually weakens with the increase of Mn ions in $YFe_{1-x}Mn_xO_3$, especially when the doping amount of Mn ions reaches 10% (S5). This is due to the structural disorder caused by the difference of radius between Mn and Fe ions. The lattice parameters according to the XRD are plotted against Mn concentration (x) as shown in Fig. S1.† The parameter a increases whereas b and c parameters decrease with the increase of Mn concentration, which is consistent with those reported in literatures.[20,28] The increase in the parameter a with the increase of Mn concentration (x) indicates the presence of Jahn–Teller distortion associated with Mn^{3+} ions.

To further explore the structure of $YFe_{1-x}Mn_xO_3$, HRTEM study was carried out, as presented in Fig. 2b. The (200), (022) and (221) planes of $YFeO_3$ is observed, which show the indistinct lattice fringe of 0.264, 0.224 and 0.186 nm space, respectively. The content of Mn element in $YFe_{1-x}Mn_xO_3$ was determined by energy dispersive spectroscopy (EDS) and increased significantly with the increase of the ratio of Mn/Fe in the precursor, achieving 3.26%, 5.95%, 12.60% and 14.10% (Fig. 2c) for the S2, S3, S4 and S5, respectively. It is worth pointing out that the experimental values of Mn content are higher than the theoretical values, which may be caused by the tendency of Mn doping to migrate to the surface of the material. In addition, EDS mappings of the $YFe_{1-x}Mn_xO_3$ showed strong and uniform signals of Mn, Fe, Y and O, as seen in Fig. 2d, and the original SEM image selected for the EDS mapping was shown in Fig. S2.† This shows that Mn ions are evenly distributed on the surface of $YFe_{1-x}Mn_xO_3$.

Fig. S3a† shows the UV-vis spectra of the $YFe_{1-x}Mn_xO_3$ materials. It is interesting to observe that the UV reflection intensity of $YFe_{1-x}Mn_xO_3$ from 250 nm to 400 nm decreased gradually with the increase of Mn doping, which means that their absorption of ultraviolet region is gradually strengthened. The UV absorption band can be primarily ascribed to electrons promotion of $YFe_{1-x}Mn_xO_3$ from the valence band to the conduction band.[35] In contrast to the pure $YFeO_3$ powder, the absorption edge of the $YFe_{1-x}Mn_xO_3$ samples displays different shifts to the visible region. This has been confirmed by roughly estimating the band gap of samples according to the plot in Fig. 3b, which is obtained via the transformation based on the Kubelka–Munk function. The estimated band gap values of S1, S2, S3, S4 and S5 are approximately 2.40, 2.35, 2.30, 2.20 and 2.02 eV, respectively, clearly showing the narrowing band gaps
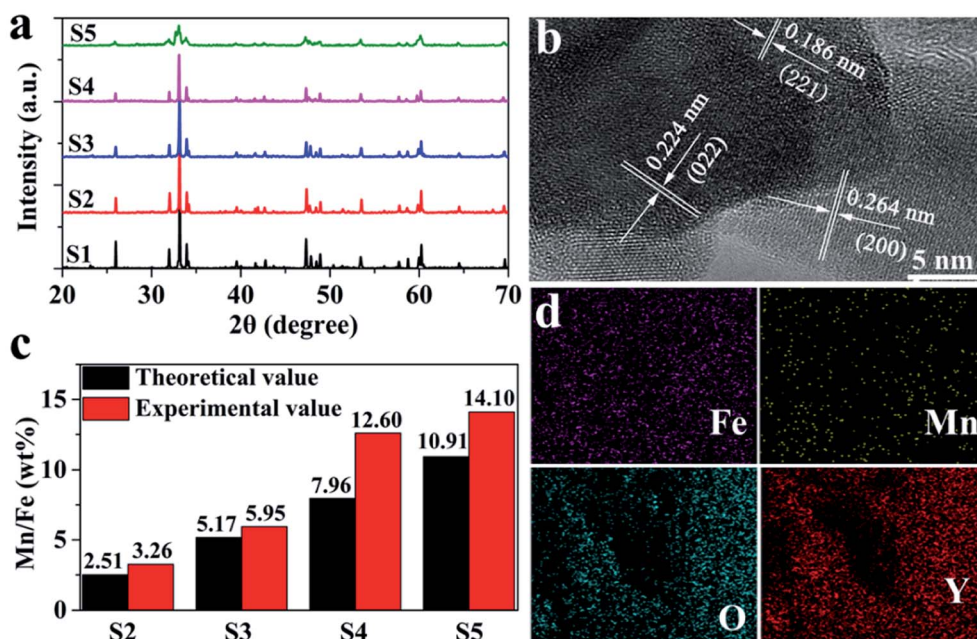

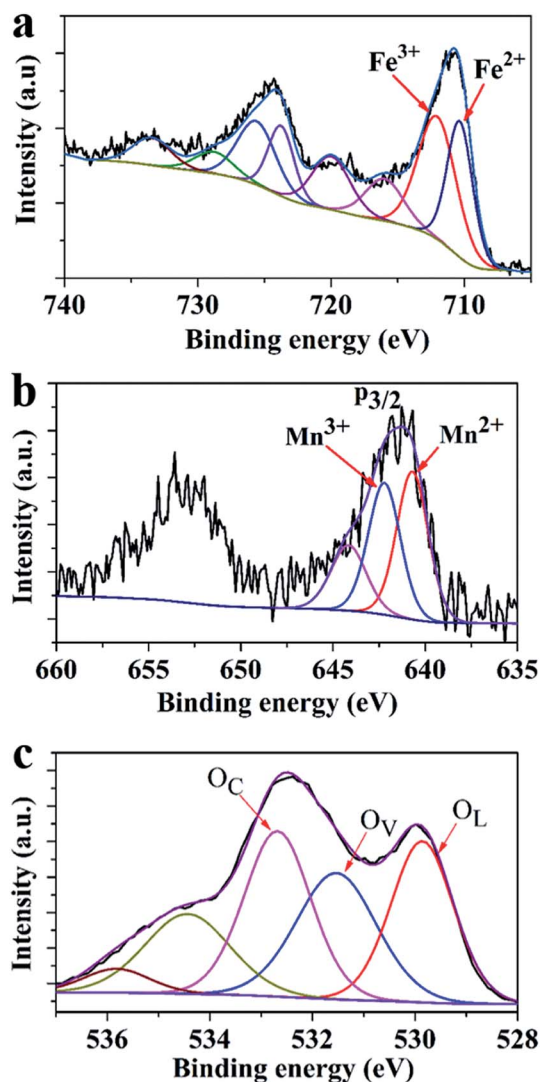Fig. 2 (a) XRD patterns, (b) HRTEM images, (c) content of Mn element in $YFe_{1-x}Mn_xO_3$ according to EDS test, and (d) EDS mappings of the samples.

Fig. 3 XPS peaks and the Gaussian fitting peaks of (a) Fe 2p, (b) Mn 2p, (c) O 1s for $YFe_{0.95}Mn_{0.05}O_3$ ($x = 0.05$) powder.

Table 1 Mass ratio of Mn to Fe calculated by XPS and ICP, and the percentage of different fitting peaks of Mn and O element

Sample	Mn/Fe[a]	Mn/Fe[b]	Mn^{3+}	Mn^{2+}	O$_C$	O$_V$	O$_L$
S1	0.0%	0.00%	0.0%	0.0%	17.2%	22.4%	60.4%
S2	3.45%	3.54%	47.7%	52.3%	22.6%	29.2%	48.2%
S3	8.41%	5.25%	48.5%	51.5%	35.3%	32.4%	32.3%
S4	10.37%	11.33%	49.2%	50.8%	26.0%	27.3%	46.7%
S5	11.29%	11.68%	52.3%	47.7%	20.5%	22.7%	56.8%

[a] Represents mass ratio of Mn to Fe calculated by XPS. [b] Represents mass ratio of Mn to Fe calculated by ICP.

and the high temperature and pressure generated during the reaction (230 °C for 72 h), the oxidation of Mn^{2+} ions will be promoted to a certain extent to produce Mn^{3+} ions. The O 1s peak data for $YFe_{0.95}Mn_{0.05}O_3$ are presented in Fig. 3c, indicating an asymmetric peak that is usually fitted with three components. The fitted peaks located at 529.9, 531.5 and 532.7 eV were labeled as O_L, O_V and O_C, respectively. O_L, O_V and O_C was associated with lattice oxygen, oxygen vacancy, and adsorbed oxygen, respectively.[38,39] For other samples, the XPS peaks of Mn, Fe with different valence states and three kinds of oxygen, and their fitting peaks are shown in Fig. S4, S5 and S6,† respectively.

The proportion of two kinds of Mn ions and oxygens is calculated according to their corresponding peak area and listed in the Table 1. It is worth noting that with the increase of doping amount of Mn ions in $YFe_{1-x}Mn_xO_3$, the proportion of Mn^{2+} ion decreases, and the proportion of Mn^{3+} ions increases. However, the increase of Mn ions in $YFe_{1-x}Mn_xO_3$ reached 3.45, 8.41, 10.37 and 11.29% for the S_2, S_3, S_4 and S_5 respectively according to XPS results, which is consistent with the ICP results (Table 1). It can be seen that the increase of Mn ions in $YFe_{1-x}Mn_xO_3$ is significantly faster than the decrease of Mn^{2+} ion. This means that although the proportion of Mn^{2+} ions decreases gradually, the net concentration of Mn^{2+} ions increases with the increase of total doping amount of Mn ions. It is well known that electronegativity is a relative scale of the ability of atoms or ions to attract electrons. The greater the electronegativity, the greater the tendency to attract electrons. The Mn^{2+} ions have lower electronegativity than the Mn^{3+} ions. In other words, Mn^{2+} ions are beneficial to the adsorption of oxygen ions on the surface of $YFe_{1-x}Mn_xO_3$, while Mn^{3+} ions are not conducive to the adsorption of oxygen ions. Thus, the competition between Mn^{2+} ions and Mn^{3+} ions may lead to the increase of oxygen ions on the surface of $YFe_{1-x}Mn_xO_3$ and then decrease (Table 1).

3.2 Fabrications and testing of sensor array

The effect of Mn doping on the gas sensing performance of $YFe_{1-x}Mn_xO_3$ is reflected by their sensing curves in Fig. 4. It can be seen from the sensing curves that $YFe_{1-x}Mn_xO_3$ with different doping concentrations has a relatively stable response to 1000 ppm of CH_2O, C_2H_6O and H_2O_2 vapors as well as 100% RH at room temperature. With the increase of Mn doping
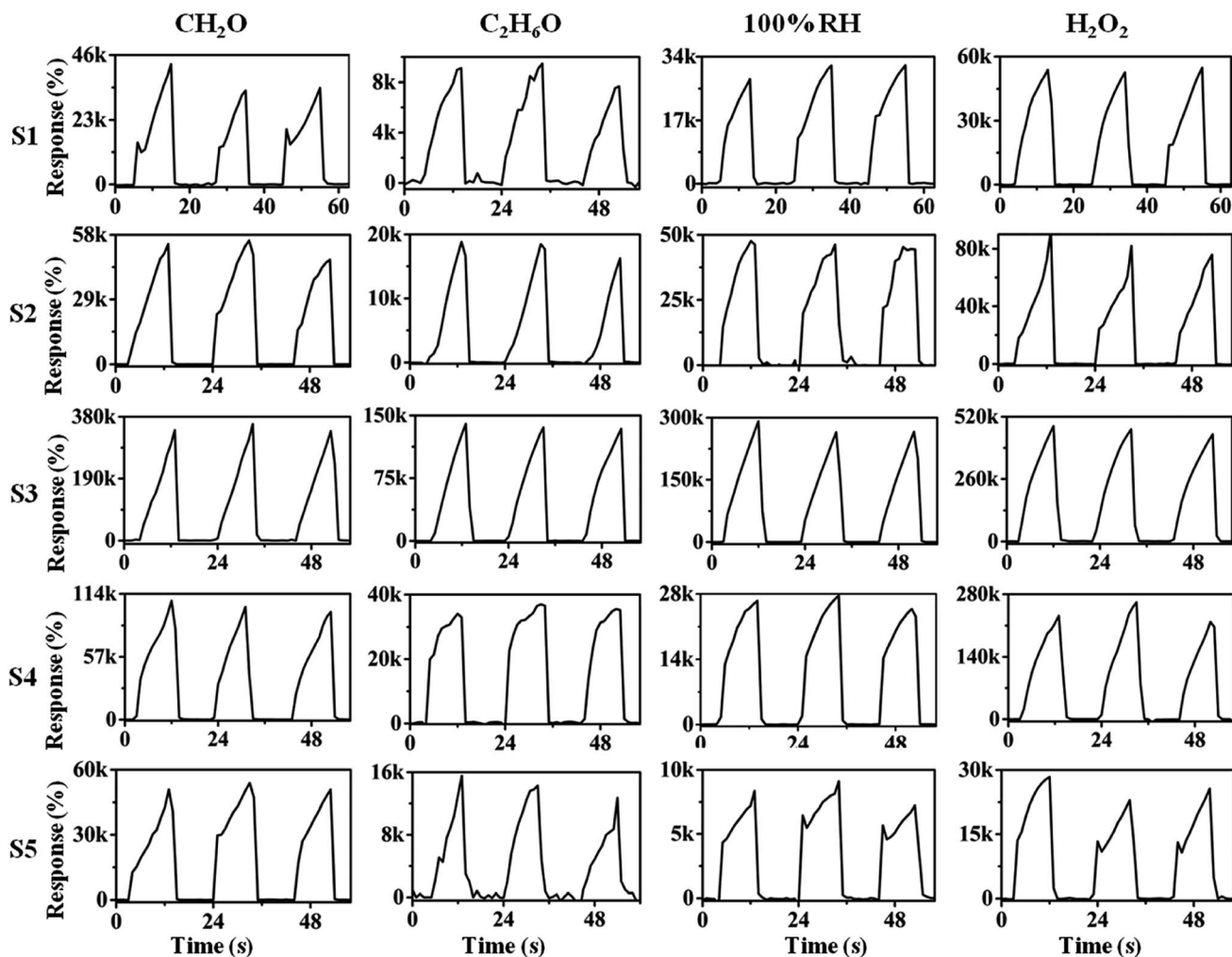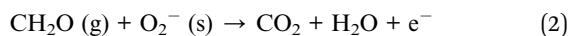
as compared to the estimated 2.40 eV of the pure $YFeO_3$. A smaller band gap means that electrons in the valence band can more easily transition to the conduction band, increasing the carrier concentration. The change of carrier concentration has an important effect on gas sensitive performance of the sensing material. Therefore, it can be concluded that Mn doping has an important effect on the gas sensitive performance of $YFe_{1-x}Mn_xO_3$.

As shown in Fig. 3a, Fe element doped in $YFe_{0.95}Mn_{0.05}O_3$ exists in mixed valence state, the Fe $2p_{3/2}$ peaks at 710.5 and 712.5 eV could be assigned to Fe^{2+} and Fe^{3+} ions, respectively.[18,36] As shown in Fig. 3b, the Mn 2p region consists of a spin–orbit doublet of Mn $2p_{3/2}$ and Mn $2p_{1/2}$, and the Mn ions doped in $YFe_{0.95}Mn_{0.05}O_3$ also exist in mixed valence state. The peaks of the Mn elements located at 640.7 and 642.5 eV correspond to Mn^{2+} and Mn^{3+} ions, respectively. These results are in good agreement with reports in the literature.[12,37] Because of the presence of Fe^{3+} ions, a small amount of oxygen in the reactor

Fig. 4   Sensing curves of different sensors based on $YFe_{1-x}Mn_xO_3$ to 1000 ppm of CH_2O, C_2H_6O, H_2O_2 and 100% RH at room temperature.

concentration, the response of $YFe_{1-x}Mn_xO_3$ to four kinds of target atmospheres first increases, then decreases. In general, the gas sensing performance of $YFe_{1-x}Mn_xO_3$ is the best when $x = 0.05$ in the $YFe_{1-x}Mn_xO_3$. In addition, it can also be seen that the $YFe_{1-x}Mn_xO_3$ after doping has the highest sensitivity to H_2O_2 vapor, followed by CH_2O vapor. When the sensor based on $YFe_{1-x}Mn_xO_3$ are exposed to CH_2O and C_2H_6O vapors, surface adsorbed oxygen (O_2^-, <100 °C; O^-, 100–300 °C; O_2^-, >300 °C) will react with CH_2O and C_2H_6O as follows,

$$CH_2O \text{ (g)} + O_2^- \text{ (s)} \rightarrow CO_2 + H_2O + e^- \tag{2}$$

$$C_2H_6O \text{ (g)} + 3O_2^- \text{ (s)} \rightarrow 2CO_2 + 3H_2O + 3e^- \tag{3}$$

In the above reactions, e^- represents a conduction electron and O_2^- (s) represents a surface adsorbed oxygen ion. CH_2O (g) and C_2H_6O (g) represents adsorbing CH_2O and C_2H_6O molecules, respectively. It can be seen that the reduced gas molecules release electrons into $YFe_{1-x}Mn_xO_3$ during the reaction and the electric current of $YFe_{1-x}Mn_xO_3$ increases quickly, which shows the sensing characteristics of n-type

semiconductor. However, the sensing signal to H_2O_2 is abnormal, which is in the same direction as the reductive gas. It is reported that H_2O_2 will react with the following two ways depending on the concentration of H_2O_2. At high H_2O_2 (of about 10 vol%) concentrations the mechanism is as follows:[40,41]

$$2H_2O_2 \rightarrow 2H_2O + O_2 \tag{4}$$
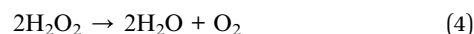
At lower concentrations (2.1 vol%) the net reaction is:

$$2H_2O_2 \rightarrow 2H_2O + 0.87O_2 + 0.08O_3 \tag{5}$$
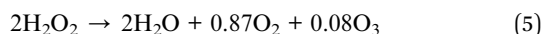
In our work, the H_2O_2 with a mass fraction of 30% was used. According to the eqn (4), the main product of H_2O_2 decomposition is H_2O and O_2. Therefore, the produced O_2 and H_2O_2 vapor will capture electrons from the $YFe_{1-x}Mn_xO_3$, and H_2O will release electrons into $YFe_{1-x}Mn_xO_3$. In this way, there is a competition between the oxidizing atmosphere and the reducing atmosphere in the sensing performance. Finally, the reductive atmosphere prevails, showing the sensing characteristics of reductive gas.

In order to better evaluate the effect of manganese doping on the sensing performance of $YFe_{1-x}Mn_xO_3$, the average responses, response time and recovery time of five sensors to four target analytes are shown in the histogram shown in Fig. S7.† From the histogram, it is clear that the response of $YFe_{1-x}Mn_xO_3$ to the target analyte increases first and then decreases with the increase of manganese doping. As shown in Fig. S7a,† the average response of S1 to 1000 ppm of CH_2O, C_2H_6O, H_2O_2 and 100% RH is 36 851%, 8750%, 51 010% and 30 441%, respectively. As for the S2, the average response to 1000 ppm of CH_2O, C_2H_6O, H_2O_2 and 100% RH is increased to 52 083%, 17 858%, 83 422% and 46 409%, respectively. However, the average response of S3 to 1000 ppm of CH_2O, C_2H_6O, H_2O_2 and 100% RH is up to 344441%, 136711%, 465226% and 274374%, respectively. Compared with the S1, the response of the S3 to 1000 ppm of CH_2O, C_2H_6O, H_2O_2 and 100% RH is increased by 835%, 1462%, 812% and 801%, respectively. When the doping amount of Mn ions increases further, the sensitivity of the $YFe_{1-x}Mn_xO_3$ begins to decrease. As a result, the response of the S4 to 1000 ppm of CH_2O, C_2H_6O, H_2O_2 and 100% RH is 92 455%, 35 380%, 237120% and 24 864%, respectively, which is still better than that of S1. It can be seen that the effect of Mn doping on the gas sensing of $YFe_{1-x}Mn_xO_3$ is obvious. In terms of response and recovery rate, Mn doping has little effect on response time and recovery time of $YFe_{1-x}Mn_xO_3$ (Fig. S7b and c†). The response time of all sensors is less than 10 s, and the recovery time is less than 2 s, reflecting the sensing characteristics of fast response and fast recovery. This is because that good crystalline quality and one dimensional structure of $YFe_{1-x}Mn_xO_3$ is accounts for the higher electron mobility in gas sensors.

Although $YFe_{1-x}Mn_xO_3$ displayed good sensitivity to the above four atmospheres, it does not show good selectivity. An obvious advantage of sensor array compared with an individual sensor is that it can realize the discriminative detection to unknown analytes, based on certain mathematical analysis, and possibly, both kinetic and thermodynamic[12,42] or PCA.[43,44] Therefore, we prepare $YFe_{1-x}Mn_xO_3$ with different Mn doping amount into a sensor array to evaluate the feasibility of forming a sensor array. The responses of sensor array to four kinds of target atmosphere are used for principal component analysis (PCA) to evaluate the performance of sensor array. As shown in the Fig. 5a, on the two-dimensional PCA diagram, the data points corresponding to CH_2O and C_2H_6O, are almost overlapped, indicating that the sensor array cannot distinguish CH_2O and C_2H_6O well. Furthermore, three-dimensional PCA (Fig. 5b) is used to evaluate the recognition ability of sensor array. Compared with the two-dimensional PCA, the three-dimensional PCA has improved the discrimination and basically achieved the discriminative detection of four analytes, but the data points corresponding to CH_2O and C_2H_6O are still relatively close. This may be because the performance of the sensors in the array is similar, so their discriminative ability is limited.

By combining the thermodynamic parameters and dynamic parameters, the digital signals can be transformed into graphic signals, and the visual detection of analytes can be realized by
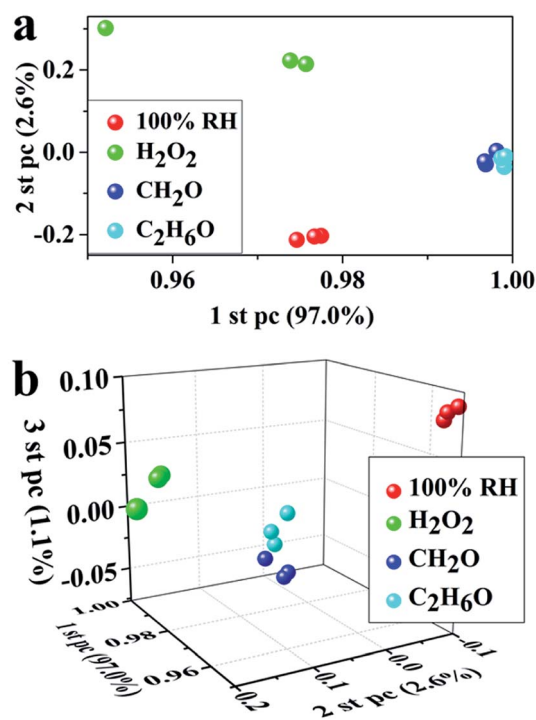

Fig. 5 (a) Two-dimensional PCA chart, (b) three-dimensional PCA chart deduced from the average responses of the sensor array containing five sensors based on $YFe_{1-x}Mn_xO_3$.

combining the image recognition technology. The response and response time are corresponding to the thermodynamic and kinetic parameters respectively. Therefore, five sensors have five response values and five response times for each analyte. For each analyte, the ratio of five responses to the corresponding five response times leads to five new parameters with thermodynamic and kinetic parameters. These five new parameters are used to build a visual pentagon and shown in Fig. 6. It can be seen from the Fig. 6 that because the S3 has the highest sensitivity, the pentagon looks like a triangle, which reduces the identification of the analyte. Therefore, we reduce the response of S3 to one tenth of the original response under the condition that other parameters remain unchanged, and build a visual pentagon again (Fig. 7). As a result, the visual recognition of four analytes is improved. Thus it can be seen if one wants to build a sensor array with high recognition ability, one need to select and optimize the sensors in the array.

Detection limit is an important parameter for estimating gas sensors. The relation between responses and vapour concentrations at RT were shown in Fig. 8. For H_2O_2 and CH_2O vapors, a nearly linear dependency between the response and the concentration in the low concentration range was observed (Fig. 8b and d). At higher concentrations, the response increases more slowly as the concentration increases, which shows that the adsorption of target molecules on the surface of sensing materials gradually reaches saturation. The linear relationship shows that the adsorption of H_2O_2 and CH_2O vapors on $YFe_{0.95}Mn_{0.05}O_3$ has not yet reached saturation in the low
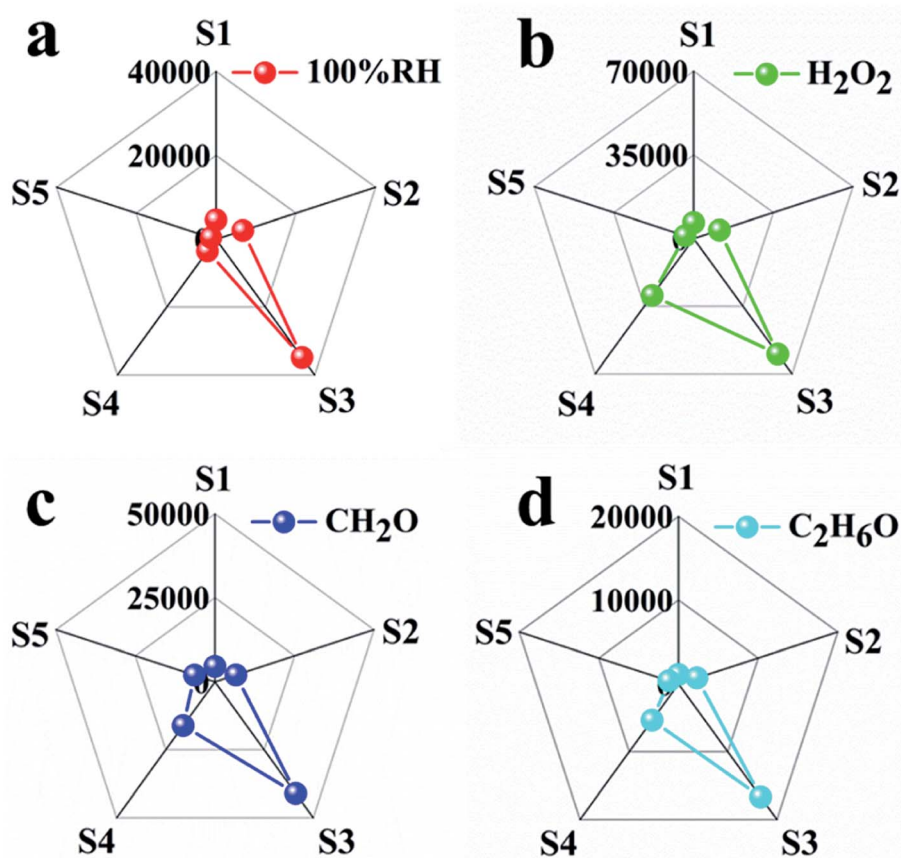
Fig. 6 Characteristic fingerprints deduced by combining kinetic and thermodynamic parameters from sensing data of (a) 100% RH, (b) saturated vapors of H_2O_2 at room temperature, (c) CH_2O, (d) C_2H_6O.

concentration range. According to the fitting results in Fig. 8b and d, the estimated LOD (defined as LOD = $3S_D/m$, where m is the slope of the linear part of the calibration curve and S_D is the standard deviation of noise in the response curve) for H_2O_2 and CH_2O is determined to be 1.75 and 2.55 ppb, respectively. These results show the high sensitivity of the $YFe_{0.95}Mn_{0.05}O_3$ to H_2O_2 and CH_2O vapors. This shows that perovskite $YFe_{1-x}Mn_xO_3$ can be used to measure both high and low concentration atmospheres and it is a very promising gas sensing materials.

According to the results of XPS analysis, with the increase of doping amount of Mn ions in $YFe_{1-x}Mn_xO_3$, the proportion of Mn^{3+} ion increases and the proportion of Mn^{2+} decreases. It can be seen that the increase of Mn ions in $YFe_{1-x}Mn_xO_3$ is significantly faster than the decrease of Mn^{2+} ion (Table 1). This means that although the proportion of Mn^{2+} ions decreases gradually, the net Mn^{2+} concentration increases with the increase of total doping amount of Mn ions. Electronegativity is a relative scale of the ability of atoms or ions to attract electrons. The Mn^{2+} ions have lower electronegativity than the Mn^{3+} ions. It means that Mn^{2+} ions are beneficial to the adsorption of oxygen ions on the surface of $YFe_{1-x}Mn_xO_3$, while Mn^{3+} ions are not conducive to the adsorption of oxygen ions. Thus, the competition between Mn^{2+} ions and Mn^{3+} ions may lead to an increase and then a decrease in the adsorbed oxygen on the surface of $YFe_{1-x}Mn_xO_3$ (Fig. 9a).

It is known that the depth of charge depletion layer (w) decide the sensing properties of chemiresistive sensors. The classical expressions for the w formed in the semiconductor upon gas adsorption:[45,46]

$$w = L_D(2\beta V_S)^{1/2} \tag{6}$$

where L_D is the Debye length, V_S the surface potential barrier, and $\beta = q/kT$, where q is the electron charge, k the Boltzmann constant, and T the temperature. While, V_S can be expressed as the following equation:[47]

$$V_S = \frac{eN_t^2}{2\varepsilon_0\varepsilon_r N_d} \tag{7}$$

where N_t is the surface density of adsorbed oxygen ions (O^{2-}, O^- or O_2^-), the $\varepsilon_r\varepsilon_0$ permittivity of the semiconductor, and N_d the carrier concentration. Clearly, the V_S value depends on temperature, atmosphere, and dopant concentration; each of these parameters influences the V_S, w and thus sensitivity.[47] Therefore, the competition between Mn^{2+} ions and Mn^{3+} ions results in the dynamic equilibrium of the oxygen absorption of the $YFe_{1-x}Mn_xO_3$ (Fig. 9a and b). XPS analysis (Table 1) shows that with the increase of Mn ions in $YFe_{1-x}Mn_xO_3$, the content of adsorbed oxygen increases first and then decreases (17.2%, 22.6%, 35.3%, 26.0% and 20.5%), reaching the maximum at $x =$
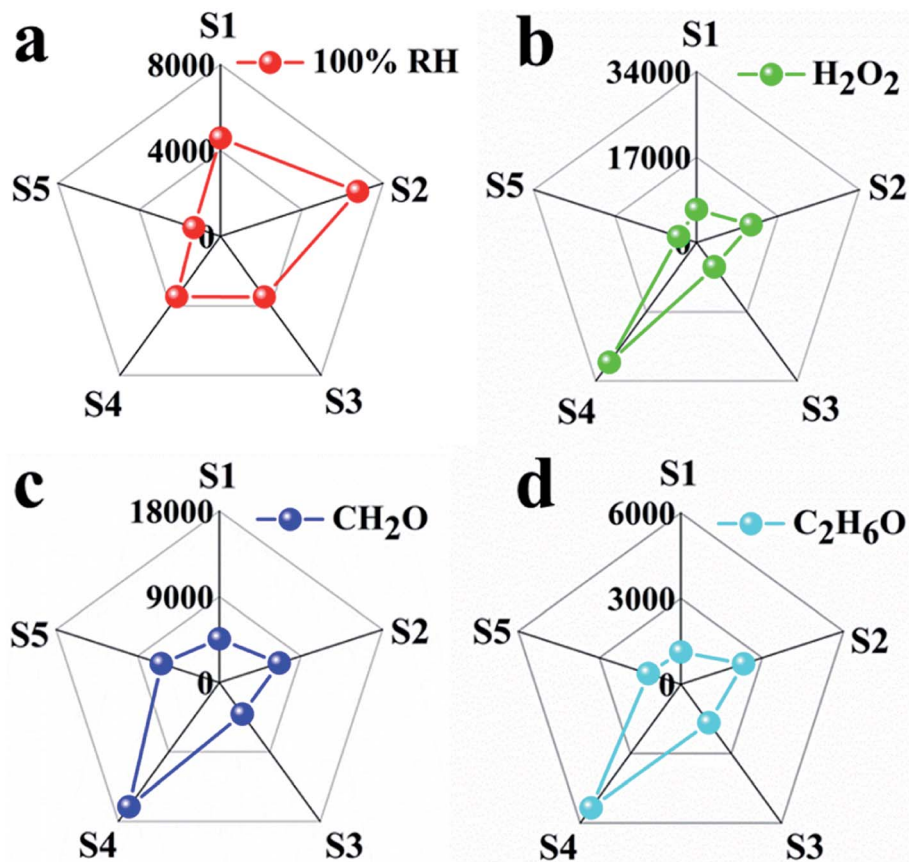
Fig. 7 Characteristic fingerprints deduced by combining kinetic and thermodynamic parameters from sensing data of (a) 100% RH, (b) saturated vapors of H_2O_2 at room temperature, (c) CH_2O, (d) C_2H_6O.
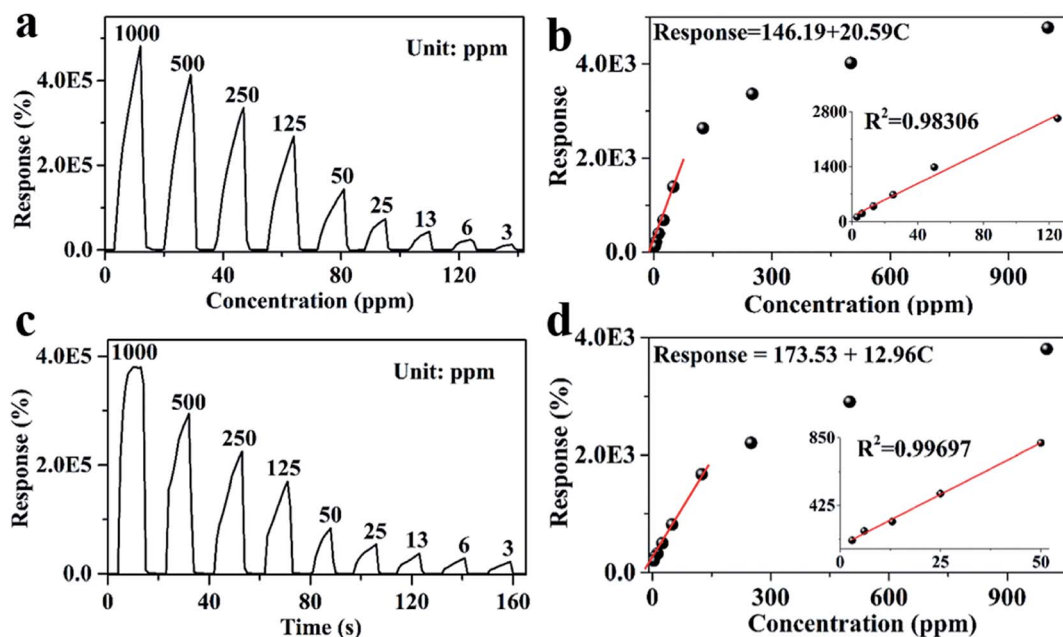

Fig. 8 Relation between responses of S3 and vapor concentrations at RT of (a) H_2O_2, (c) CH_2O; the fitting plots of response *vs.* concentration of (b) H_2O_2, (d) CH_2O.
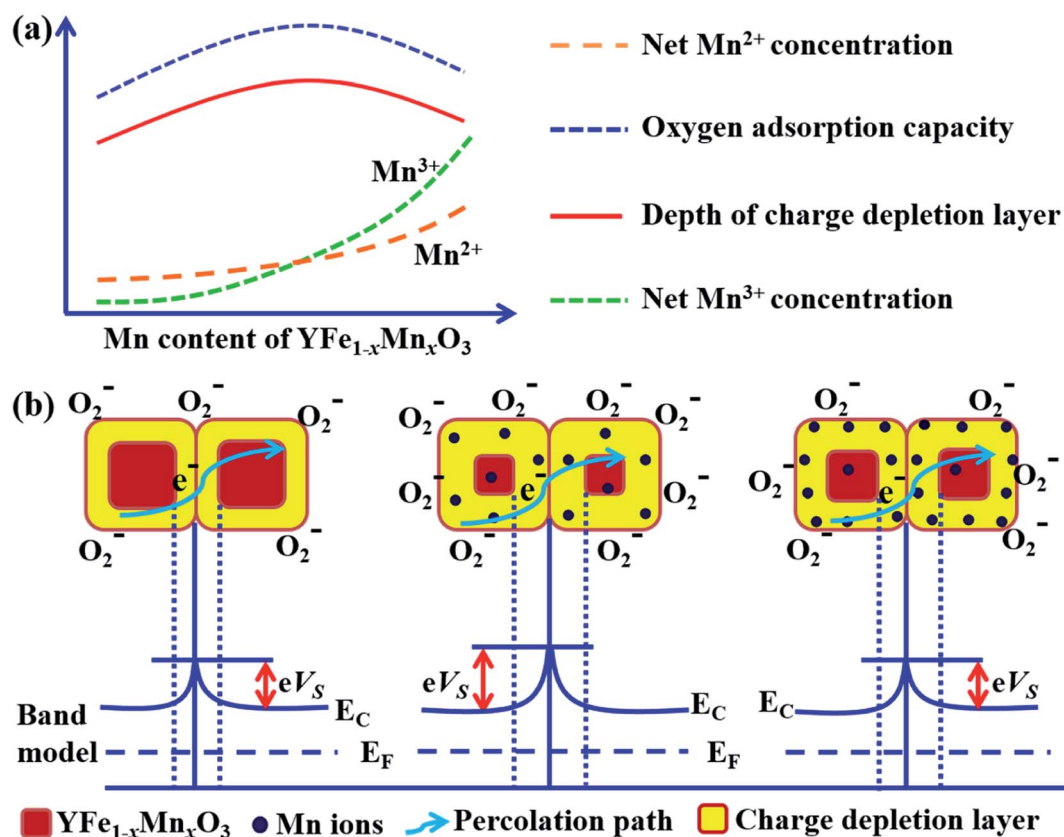
Fig. 9 (a) The variation of net Mn^{2+} and Mn^{3+} concentrations with the increase of Mn doping, and the influence on oxygen adsorption capacity and the charge depletion layer, (b) structural and band models showing the role of Mn doping of the charge depletion layer of $YFe_{1-x}Mn_xO_3$.

0.05 for $YFe_{1-x}Mn_xO_3$. In addition, the increasing defects of $YFe_{1-x}Mn_xO_3$ caused by the doping of Mn ions may reduce the adsorption efficiency of oxygen ions for $YFe_{1-x}Mn_xO_3$, contributing to the tendency of first increase and then decrease of adsorbed oxygen. Accordingly, with the increase of Mn ions, the charge depletion layer of the material also increases first and then decreases (Fig. 9b). Therefore, the sensing performance of $YFe_{1-x}Mn_xO_3$ is the best when $x = 0.05$. When the w is constant, the wider the width of the basic unit quadprism, the lower the proportion of w in the whole quadprism, also resulting in the lower sensitivity. The dynamic equilibrium results in the increase of gas sensing properties of $YFe_{1-x}Mn_xO_3$ first and then decrease, which means that the doping of Mn ions can effectively control the gas sensing properties of $YFe_{1-x}Mn_xO_3$.

4. Conclusion

Perovskite $YFe_{1-x}Mn_xO_3$ with hierarchical structure was prepared by simple hydrothermal method and used as gas sensing materials. The gas sensing test showed that $YFe_{1-x}Mn_xO_3$ with different Mn doping amount displayed fast response and recovery characteristics to multiple target analytes as well as the good stability and recoverability. With the increase of Mn doping concentration, the response of $YFe_{1-x}Mn_xO_3$ to four kinds of target atmospheres first increases, then decreases. The gas sensing performance of $YFe_{1-x}Mn_xO_3$ is the best when $x = 0.05$. Compared with the S1, the response of the

S3 to 1000 ppm of CH_2O, C_2H_6O, H_2O_2 and 100% RH is increased by 835%, 1462%, 812% and 801%, respectively. According to the PCA and radar chart analysis, the sensor array based on $YFe_{1-x}Mn_xO_3$ can basically identify four kinds of target analytes, and shows higher recognition ability after further data processing. It is feasible to realize the visual and discriminative detection of the target analyte by constructing sensor array through radar chart analysis and database construction.

Conflicts of interest

The authors declare no conflict of interest.

Acknowledgements

References

1 L. Malavasi, C. Tealdi, G. Flor, G. Chiodelli, V. Cervetto, A. Montenero and M. Borella, *Sens. Actuators, B*, 2005, **105**, 407–411.

2 Y. Yin, N. Zhang, J. Han, C. Liu, S. Adimi, S. Wen, X. Li and S. Ruan, *Sens. Actuators, B*, 2019, **297**, 126738.

3 V. Chumakova, A. V. Marikutsa, M. N. Rumyantseva, D. Fasquelle and A. M. Gaskov, *Sens. Actuators, B*, 2019, **296**, 126661.

4 J. W. Fergus, *Sens. Actuators, B*, 2007, **123**, 1169–1179.

5 H. Saoudi, A. Benali, M. Bejar, E. Dhahri, T. Fiorido, K. Aguir and R. Hayn, *J. Alloys Compd.*, 2018, **731**, 655–661.

6 S. Smiy, H. Saoudi, A. Benali, M. Bejar, E. Dhahri, T. Fiorido and K. Aguir, *Chem. Phys. Lett.*, 2019, **735**, 136765.

7 J. Cerdà, J. Arbiol, G. Dezanneau, R. Díaz and J. R. Morante, *Sens. Actuators, B*, 2002, **84**, 21–25.

8 G. Martinelli, M. C. Carotta, M. Ferroni, Y. Sadaoka and E. Traversa, *Sens. Actuators, B*, 1999, **55**, 99–110.

9 Y. Hu, O. K. Tan, J. S. Pan, H. Huang and W. Cao, *Sens. Actuators, B*, 2005, **108**, 244–249.

10 H. Ying, T. Ooi Kiang, C. Wenqing and Z. Weiguang, *IEEE Sens. J.*, 2005, **5**, 825–832.

11 G. G. Mandayo, F. González, I. Rivas, I. Ayerdi and J. Herrán, *Sens. Actuators, B*, 2006, **118**, 305–310.

12 Z. Wu, C. Zhou, B. Zu, Y. Li and X. Dou, *Adv. Funct. Mater.*, 2016, **26**, 4578–4586.

13 L. Shao, Z. Wu, H. Duan and T. Shaymurat, *Sens. Actuators, B*, 2018, **258**, 937–946.

14 A. Rothschild, S. J. Litzelman, H. L. Tuller, W. Menesklou, T. Schneider and E. Ivers-Tiffée, *Sens. Actuators, B*, 2005, **108**, 223–230.

15 V. I. Popkov, O. V. Almjasheva, A. S. Semenova, D. G. Kellerman, V. N. Nevedomskiy and V. V. Gusarov, *J. Mater. Sci.: Mater. Electron.*, 2017, **28**, 7163–7170.

16 A. V. Racu, D. Ursu, O. V. Kuliukova, C. Logofatu, A. Leca and M. Miclau, *Mater. Lett.*, 2015, **140**, 107–110.

17 Z. Lazarevic, C. Jovalekic, M. Gilic, V. N. Ivanovski, A. Umicevic, D. L. Sekulic and Z. N. Romcevic, *Sci. Sintering*, 2017, **49**, 277–284.

18 S. Jabbarzare, M. Abdellahi, H. Ghayour, A. Chami and S. Hejazian, *J. Alloys Compd.*, 2016, **688**, 1125–1130.

19 M. P. F. Graca, L. C. Costa, F. Amaral, M. A. Valente, W. M. Barcellos, F. N. A. Freire, K. D. A. Saboia and A. S. B. Sombra, *Spectrosc. Lett.*, 2017, **50**, 206–213.

20 P. Mandal, C. Serrao, E. Suard, V. Caignaert, B. Raveau, A. Sundaresan and C. N. R. Rao, *J. Solid State Chem.*, 2013, **197**, 408–413.

21 C. Zhang, H. Yan, X. Wang, Z. Wang, H. Li and L. Li, *Ceram. Int.*, 2017, **43**, 17216–17219.

22 S. C. Haw, C. Y. Kuo, Z. Hu, J. W. Lin, J. M. Lee, K. Lu, C. Lee, H. J. Lin, J. F. Lee and C. W. Pao, *J. Alloys Compd.*, 2019, **780**, 79–84.

23 Z. Yang, Y. Huang, G. Chen, Z. Guo, S. Cheng and S. Huang, *Sens. Actuators, B*, 2009, **140**, 549–556.

24 D. Zhang, C. Jiang and J. Wu, *Sens. Actuators, B*, 2018, **273**, 176–184.

25 Q. Sun, Z. Wu, H. Duan and D. Jia, *Sensors*, 2019, **19**, 1281.

26 D. J. Norris, A. L. Efros and S. C. Erwin, *Science*, 2008, **319**, 1776.

27 G. Korotcenkov, *Sens. Actuators, B*, 2005, **107**, 209–232.

28 B. Deka, S. Ravi, A. Perumal and D. Pamu, *Ceram. Int.*, 2017, **43**, 1323–1334.

29 A. T. Nguyen, V. N. T. Pham, T. T. L. Nguyen, V. O. Mittova, Q. M. Vo, M. V. Berezhnaya, I. Y. Mittova, T. H. Do and H. D. Chau, *Solid State Sci.*, 2019, **96**, 105922.

30 Z. Yang and X. Dou, *Adv. Funct. Mater.*, 2016, **26**, 2406–2425.

31 T. Shaymurat, Q. Tang, Y. Tong, L. Dong and Y. Liu, *Adv. Mater.*, 2013, **25**, 2269–2273.

32 Z. M. Xiao, L. B. Kong, S. Ruan, X. Li, S. Yu, X. Li, Y. Jiang, Z. Yao, S. Ye and C. Wang, *Sens. Actuators, B*, 2018, **274**, 235–267.

33 M. Shang, C. Zhang, T. Zhang, L. Yuan, L. Ge, H. Yuan and S. Feng, *Appl. Phys. Lett.*, 2013, **102**, 062903.

34 O. Rosalesgonzalez, F. S. Jesus, C. A. Cortesescobedo and A. M. Bolarinmiro, *Ceram. Int.*, 2018, **44**, 15298–15303.

35 N. Zhang, S. Liu, X. Fu and Y. Xu, *J. Phys. Chem. C*, 2011, **115**, 9136–9145.

36 Y. Tang, L. Liu, H. Zhao, Y. Zhang, L. B. Kong, S. Gao, X. Li, L. Wang and D. Jia, *ACS Appl. Mater. Interfaces*, 2018, **10**, 20225–20230.

37 Z. Zeng, H. Zhou, X. Long, E. Guo and X. Wang, *J. Alloys Compd.*, 2015, **632**, 376–385.

38 M. Dai, L. Zhao, H. Gao, P. Sun, F. Liu, S. Zhang, K. Shimanoe, N. Yamazoe and G. Lu, *ACS Appl. Mater. Interfaces*, 2017, **9**, 8919–8928.

39 S. YıLmaz, S. Garry, E. McGlynn and E. Bacaksiz, *Ceram. Int.*, 2014, **40**, 7753–7759.

40 N. Näther, H. Henkel, A. Schneider and M. J. Schöning, *Phys. Status Solidi A*, 2009, **206**, 449–454.

41 E. Capua, R. Cao, C. N. Sukenik and R. Naaman, *Sens. Actuators, B*, 2009, **140**, 122–127.

42 A. Lichtenstein, E. Havivi, R. Shacham, E. Hahamy, R. Leibovich, A. Pevzner, V. Krivitsky, G. Davivi, I. Presman and R. Elnathan, *Nat. Commun.*, 2014, **5**, 4195.

43 Q. Sun, Z. Wu, Y. Cao, J. Guo, M. Long, H. Duan and D. Jia, *Sens. Actuators, B*, 2019, **297**, 126689.

44 Z. Chen, Y. Yang, Y. Xie, B. Guo and Z. Hu, *Sens. Actuators, A*, 2013, **201**, 66–72.

45 N. Yamazoe and K. Shimanoe, *Sens. Actuators, B*, 2008, **128**, 566–573.

46 M. Epifani, J. D. Prades, E. Comini, E. Pellicer, M. Avella, P. Siciliano, G. Faglia, A. Cirera, R. Scotti and F. Morazzoni, *J. Phys. Chem. C*, 2008, **112**, 19540–19546.

47 G. Zhang and M. Liu, *Sens. Actuators, B*, 2000, **69**, 144–152.